

## Electronic consequences of lateral composition modulation in semiconductor alloys

T. Mattila, L.-W. Wang, and Alex Zunger\*

National Renewable Energy Laboratory, Golden, Colorado 80401

(Received 16 November 1998)

Lateral composition modulation (CM) is a periodic, position-dependent variation in alloy composition occurring in the substrate plane, perpendicular to the growth direction. It can be induced by growing size-mismatched short-period AC/BC superlattices (SL). Here we study the electronic structure induced by such lateral composition modulation in GaAs/InAs, GaP/InP, and AlP/GaP, in search of optical properties relative to the corresponding random alloys. We investigate in detail the properties of (a) pure CM without any SL, (b) pure SL without any CM, and (c) the combined CM+SL system. The systems are modeled by constructing a large supercell where the cation sublattice sites are randomly occupied in the lateral (vertical) direction according to the composition variation induced by CM (SL). The atomic structure and strain induced by CM and SL are explicitly taken into account using an *atomistic* force field. This approach is found to be crucial for an accurate description of the microscopic strain in CM+SL systems. The electronic structure is solved using specially constructed empirical pseudopotentials and plane-wave expansion of the wave functions. We find that (i) CM in GaAs/InAs and GaP/InP systems induces type-I band alignment (electrons and holes localized in the same spatial region), while CM in AlP/GaP is shown as an example exhibiting type-II band alignment. (ii) CM and SL both induce significant contributions (which add up nearly linearly) to band-gap redshift with respect to random alloy. CM in GaP/InP is found to induce larger band-gap redshifts than in GaAs/InAs due to larger band offsets in the former system. (iii) The symmetry of electronic states at the valence band maximum is sensitively affected by CM: the lowest energy optical transitions exhibit strong polarization where transitions polarized perpendicular to the CM are favored, while transitions polarized parallel to the CM are suppressed by being shifted to higher energy. These observations, as well as the magnitude of the predicted band-gap redshift, agree with available experimental data, and suggest that control of composition modulation during growth might be used to tailor band gaps, carrier localization, and transition polarizations relative to random alloys. [S0163-1829(99)02824-6]

### I. INTRODUCTION

Lateral composition modulation (CM) is a periodic, position-dependent variation in alloy composition occurring in the substrate plane, perpendicular to the growth direction.<sup>1</sup> It has been observed in two leading growth modes: (i) in *homogeneously grown* alloy samples, i.e., where all alloy elements are deposited simultaneously on the substrate. This includes lattice-matched liquid-phase epitaxy (LPE) samples [e.g., InGaAsP (Refs. 2,3)] and molecular beam epitaxy (MBE) growth of  $\text{Ga}_{1-x}\text{Al}_x\text{As}$  on vicinal (001) GaAs substrate;<sup>4</sup> (ii) in *sequential growth*, e.g., in (001) MBE grown *short-period superlattices* of GaP/InP,<sup>5-8</sup> GaAs/InAs,<sup>9-11</sup> or AlAs/InAs,<sup>11-13</sup> on lattice-matched (001) buffer substrates. The *lateral* composition modulation is distinct from the *vertical* [001] platelet modulation occurring in growth of, e.g.,  $\text{In}_x\text{As}_{1-x}\text{Sb}$ ,<sup>14</sup> or  $\text{In}_x\text{Al}_{1-x}\text{As}$ ,<sup>15</sup> or from the CuPt-like spontaneous ordering<sup>1</sup> occurring along the [111] direction with monolayer periodicity.

Most recent studies have concentrated on type (ii) growth mode (sequential growth).<sup>5-13</sup> Here one grows a [001]-oriented  $(\text{AC})_n/(\text{BC})_m$  short-period ( $n, m \sim 1-2$ ) superlattice-with lattice mismatched constituents  $a_{\text{AC}} \neq a_{\text{BC}}$  on a substrate that is matched to the global in-plane superlattice dimensions. If the growth is initiated, for example, with AC, this material would form initially a wetting layer, and subsequently islands (if the AC thickness exceeds a critical thickness for Stranski-Krastanov growth). Depending on

the growth conditions (e.g., substrate orientation, choice of superlattice and substrate materials, etc.) these islands could (a) develop in a single substrate orientation, giving rise to a wirelike structure (“one-dimensional composition modulation”),<sup>5,6,8-12,16</sup> or (b) vertically self-align due to their strain fields,<sup>17</sup> giving rise to a dot array (also called “two-dimensional composition modulation”).<sup>13,16,18</sup> In both cases, the *lateral* composition modulation is thus *spontaneously* generated during the intentional growth of *vertical* short-period superlattices. Although CM is experimentally commonly observed in short-period superlattice systems, a complete picture of its origin is not yet fully resolved. It is evident that the strain-induced lateral ordering of nucleating islands<sup>6,9,10</sup> plays an important role in the formation process. However, the connection to continuum elasticity models, which predict morphological instability for strained alloy layers,<sup>19</sup> stress-driven alloy decomposition,<sup>20</sup> and composition fluctuations due to kinetic effects<sup>21</sup> is not well established.

Instead of trying to resolve the mechanisms causing CM, in this paper we concentrate on the electronic consequences of type (a) one-dimensional CM, while in a future publication we will model type (b) two-dimensional CM (dot array). The position-dependent modulation in composition  $x(\vec{R})$  about an average composition  $x_0$  is taken to have the general form

$$x(\vec{R}) = x_0 + A f_{\lambda, \vec{u}}(\vec{R}), \quad (1)$$

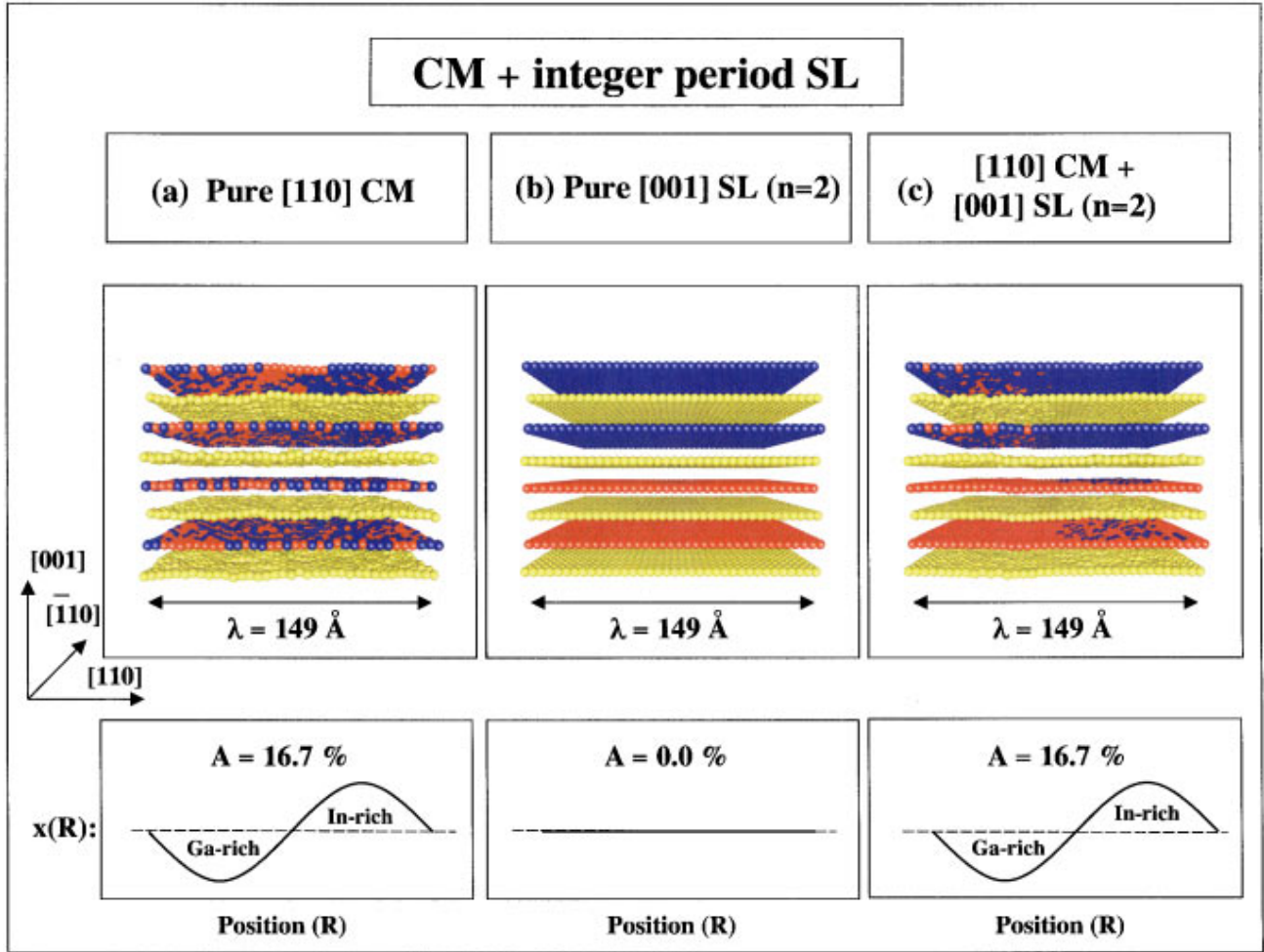


FIG. 1. (Color) The atomic structure of (i) pure [110] composition modulation, (ii) pure [001] *integer* period ( $n=2$ ) superlattice, and (iii) the combination of (i) and (ii). The red (blue) spheres represent Ga (In) atoms while As atoms are shown in yellow.

where  $A$  is the amplitude,  $\lambda$  is the wavelength and  $\vec{u}$  is a vector along the direction of the modulation. For III-V semiconductor alloys,  $\lambda \approx 100-200 \text{ \AA}$ , and  $A \approx 1-20\%$ , depending on growth conditions.<sup>5,6,8-13</sup> The function  $f_{\lambda, \vec{u}}$  is a rounded square wave or sinusoidal, e.g.,  $f_{\lambda, \vec{u}}(\vec{R}) = \sin[(2\pi\vec{R} \cdot \vec{u})/\lambda]$ . In most of the experimentally studied systems  $\vec{u}$  is along  $[\bar{1}10]$  or  $[110]$ .<sup>5,6,8-13</sup>

Figure 1 illustrates, for InAs/GaAs, the structures of (a) lateral [110] alloy CM of  $\text{In}_x\text{Ga}_{1-x}\text{As}$  without any superlattice (SL) structure [Eq. (1)], (b) pure [001] SL, and (c) a combination of both. The atomic positions were calculated by minimizing the strain energy, as explained in Sec. II A. In the [001] superlattice [Fig. 1(b)] the atomic layer sequence consists of two InAs monolayers followed by two monolayers of GaAs. We see that a combination of [001] SL with [110] oriented lateral CM [Fig. 1(a)] results [Fig. 1(c)] in the wirelike structure. Experimental studies have shown that the strongest lateral CM is observed when the deposited superlattice layers have *noninteger* values, i.e., for  $(AC)_n/(BC)_m$  superlattice ( $n, m \neq 1, 2, \dots$ ).<sup>9,11-13</sup> An example of such *fractional period* [001] SL ( $n=m=1.5$ ) and its combination with the lateral CM wave is shown in Fig. 2. In the fractional ( $n=1.5$ ) period superlattice the layer sequence consists of a full monolayer of InAs, followed by an alloy monolayer of InGaAs, where the cation sublattice is randomly occupied by

Ga and In atoms, and finally a full monolayer of GaAs. This can result from epitaxial growth experiments where one first grows 1.5 monolayers of InAs followed by the growth of 1.5 monolayers of GaAs. If the mixed alloy layer that is sandwiched between the binary layers of GaAs and InAs segregates, CM is automatically induced provided that a vertical alignment occurs between the successive mixed layers similar to self-alignment of quantum dot arrays.<sup>17</sup> Such a structure with sinusoidal lateral segregation is shown in Fig. 2(c). We note that the crucial difference between the  $n=2$  and  $n=1.5$  SL + CM systems is that while for  $n=2$  SL we have to induce atomic substitution in the pure layers to obtain a lateral CM wave, in the case of  $n=1.5$  SL the lateral CM can be simply generated by assuming rearrangement of cations in the mixed alloy layer while keeping the pure layers intact.

It is evident that the strain fields induced by the [001] SL and [110] CM can interact in a complex manner. The purpose of this paper is to study the electronic consequences of such a combined compositional and strain waves. Our aim is to see how (i) the composition wave amplitude  $A$ , (ii) the wave's orientation  $\vec{u}$ , and (iii) its wavelengths  $\lambda$  affect (a) the band-gap, (b) wave function localization (type I or II), (c) valence band splitting, and (d) polarization selection rules. To gain insight into the governing effects in the electronic structure of the combined CM+SL system, we study separately pure CM and pure SL systems.

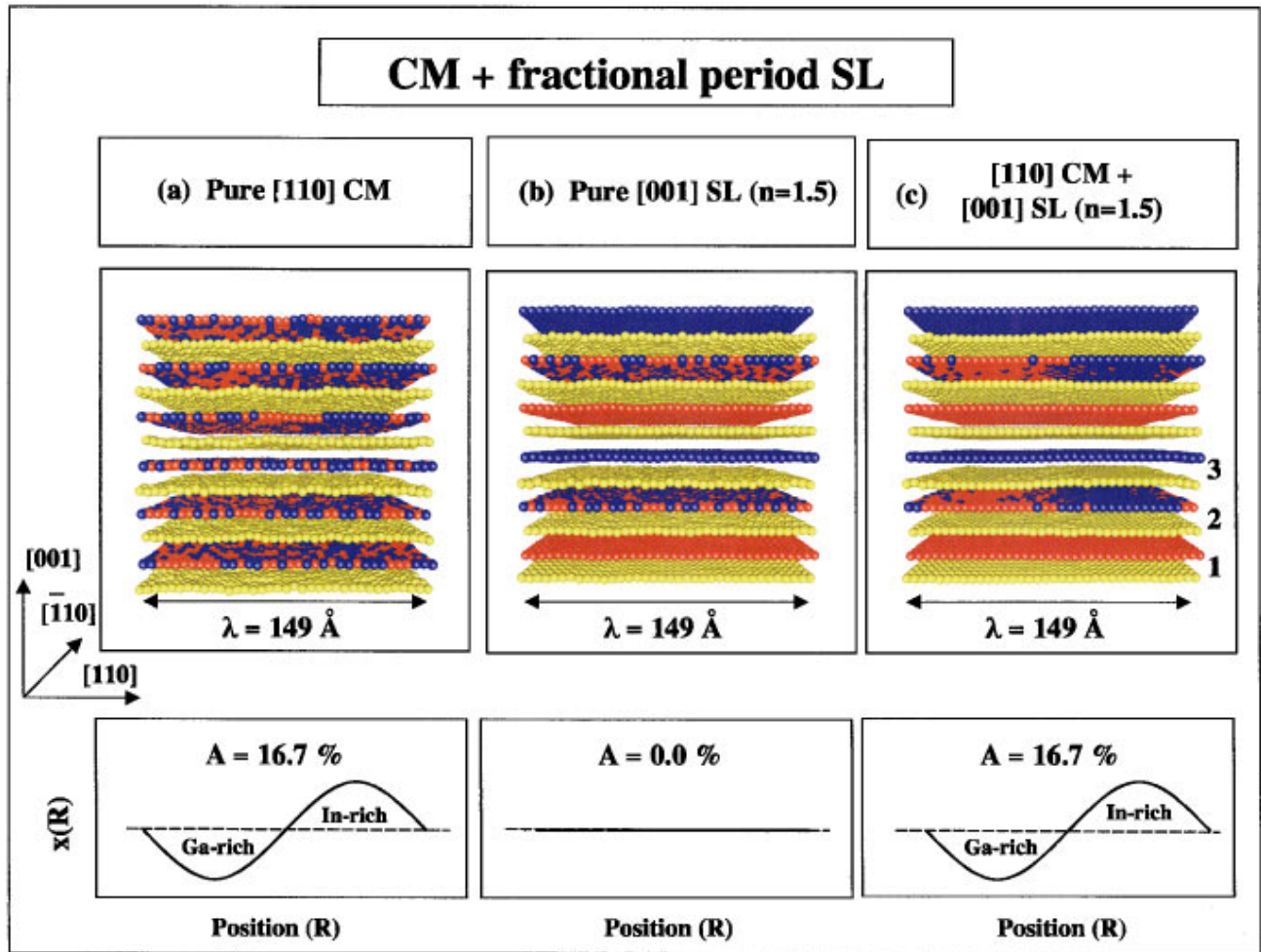


FIG. 2. (Color) The atomic structure of (i) pure [110] composition modulation, (ii) pure [001] fractional period ( $n=1.5$ ) superlattice, and (iii) the combination of (i) and (ii). The red (blue) spheres represent Ga (In) atoms while As atoms are shown in yellow. The labeling of atomic layers used in Fig. 7 is shown in panel (c).

There are three previous attempts at modeling the electronic structure of CM+SL systems: by Mascarenhas *et al.*,<sup>8</sup> by Rich *et al.*,<sup>7</sup> and by Zhang and Mascarenhas.<sup>22</sup> We have recently presented<sup>23</sup> an *atomistic* study of CM+SL. There are several reasons why atomistic study is needed here: (1) The problem involves a substitutional alloy, which cannot be described accurately by continuum models, especially when composition fluctuations<sup>24</sup> or ordering exist. (2) Short-period ( $n \sim 2$ ) SL exists in the system. It has been shown<sup>25</sup> that the continuum effective mass or  $\mathbf{k} \cdot \mathbf{p}$  model cannot be used to describe the electronic structure of a short-period SL. (3) Microscopic strain plays an important part in the problem. As will be shown below (Sec. III B) the continuum models are not able to describe the microscopic strain accurately. However, a large system size ( $\sim 10^4$  atoms) is required in the atomistic approach, since the cell has to incorporate one complete CM wavelength ( $\lambda \sim 100 - 200 \text{ \AA}$ ) in one direction, and simultaneously, in the directions perpendicular to the CM wave, be large enough to allow realistic random occupation of the alloyed sublattice sites. Therefore, special techniques (see Sec. II) for solving the minimized atomic and electronic structure have to be applied. We next outline the main differences between our approach and the earlier studies.<sup>8,7,22</sup>

To study effects (i)–(iii) on properties (a)–(d) one needs to consider the following questions: (1) what type of strain field is set up by the concomitant existence of a composition wave along  $\vec{u}$  and the SL along [001]; (2) how does this strain field couple to the electronic structure; and (3) how to represent and solve the ensuing electronic structure problem.

Problem (1) will be addressed here by applying *atomistic elasticity* theory, namely the valence force field method,<sup>26</sup> to minimize the strain energy associated with each assumed CM+SL configuration. Arbitrary strain configurations are thus treated directly. Previous approaches<sup>8,7,22</sup> ignored the explicit [001] strain due to SL and assumed that for thick films the CM strain can be approximated by the harmonic continuum elasticity. In Sec. III B we will compare the atomistic and continuum approaches to determine the strain in the CM and CM+SL systems. We find that (i) for systems having no SL, i.e., ‘‘pure CM,’’ atomistic and continuum approaches give nearly identical strain, but (ii) for the CM+SL system the strain given by atomistic elasticity for individual monolayers differs considerably from that given by the continuum approach. This indicates that for a realistic description of strain in the CM+SL system an *atomistic* approach is necessary.

Problem (2) will be addressed by using specially constructed atomic pseudopotentials which have explicit dependence on the local strain. These pseudopotentials are fitted to reproduce bulk band structures, hydrostatic and biaxial deformation potentials, and natural and biaxially strained band offsets based on available experimental and theoretical (first-principles local-density approximation method) data. Thus, the coupling of atomic displacements to the electronic structure is described atomically and explicitly. In earlier studies<sup>8,7,22</sup> the atomic degrees of freedom were coupled to electronic structure rather approximately using a continuum strain-dependent  $\mathbf{k} \cdot \mathbf{p}$  Hamiltonian. This has resulted in some ambiguity in the band alignment in CM systems: the studies by Mascarenhas *et al.*<sup>8</sup> and Tang *et al.*<sup>7</sup> model CM in  $\text{Ga}_{1-x}\text{In}_x\text{P}$  as a piecewise constant effective-mass superlattice and find a type-II alignment between Ga-rich and In-rich regions. This led to the prediction that CM in  $\text{Ga}_{1-x}\text{In}_x\text{P}$  will spatially separate electrons and holes, and to the proposal of a new solar cell device structure based on this effect<sup>27</sup>. In the more recent study, Zhang and Mascarenhas<sup>22</sup> used a multi-band  $\mathbf{k} \cdot \mathbf{p}$  method with spatially varying effective potential. They find this time a type-I alignment with no electron-hole separation for all CM systems ( $\text{Ga}_{1-x}\text{In}_x\text{P}$ ,  $\text{Ga}_{1-x}\text{In}_x\text{As}$ ,  $\text{Al}_x\text{In}_{1-x}\text{As}$ ) covered in their study. It would be desirable to determine more rigorously whether or not CM leads to electron-hole separation.

Problem (3) will be solved by a general expansion of the wave function in plane waves and a direct diagonalization of the pseudopotential Hamiltonian in this basis. Thus, the effects of the SL of CM are included directly, no effective-mass approximation is used (particularly questionable for short-period, 1–2 monolayer, superlattices<sup>25</sup>) and a multi-band coupling is allowed. Previous studies of CM (Refs. 8,7 and 22) have relied on their approach on the effective-mass theory. Mascarenhas *et al.*<sup>8</sup> and Tang *et al.*<sup>7</sup> ignored the potential-energy modulation along the CM direction, and included a kinetic-energy modulation via variation of the effective mass. Furthermore, the SL was not considered directly; its effect was included indirectly and partially by including a crystal-field splitting for the pseudo-alloy describing the SL. Ref. 22 included the SL via the anticipated crystal-field splitting it causes, but ignored the electronic structure of the SL (e.g., the  $\Gamma$ – $X$  coupling it causes) or the Hamiltonian coupling of the SL with the CM.

Our main results are:

(i) CM in GaP/InP and GaAs/InAs shows type-I band alignment (electrons and holes localized in the same spatial region). Inclusion of a vertical SL does not alter the band alignment. We use AlP/GaP as an example of a system exhibiting a type-II alignment.

(ii) Both CM and SL induce significant band gap redshifts with respect to the random alloy. In a combined CM+SL system their contributions add up nearly linearly: for  $A = 8\%$  we find  $\Delta E_{\text{gap}} = -40(-215)$  meV in  $\text{Ga}_{1-x}\text{In}_x\text{As}$  ( $\text{Ga}_{1-x}\text{In}_x\text{P}$ ), of which the SL contribution is  $\sim -20(-130)$  meV.

(iii) The lowest energy transitions between the conduction and valence states are distinctly polarized due to CM and SL: the transitions polarized along the composition wave (lateral for CM and vertical for SL) are suppressed by being shifted to higher energy. In the combined CM+SL system CM and

SL act as sequential filters. The CM+SL system in  $\text{Al}_x\text{Ga}_{1-x}\text{P}$  is found to have an indirect band gap (in reciprocal space), limiting its use in practical optical applications.

This study thus shows that if one were able to control growth parameters to select desirable CM amplitude ( $A$ ) and wavelength ( $\lambda$ ) it would be possible to tailor the optical properties of semiconductor alloys in a significant way.

## II. METHOD OF CALCULATION

We wish to solve the Schrödinger equation

$$\left\{ -\frac{1}{2}\nabla^2 + \sum_{\alpha,m} v_{\alpha}(\mathbf{r}-\mathbf{R}_{\alpha,m}) \right\} \psi_i(\mathbf{r}) = \epsilon_i \psi_i(\mathbf{r}), \quad (2)$$

where  $\mathbf{R}_{\alpha,m}$  are the atomic positions ( $\alpha$  denotes atomic species and  $m$  runs over individual atoms) and  $v_{\alpha}$  is the screened atomic pseudopotential. In order to obtain the electronic structure given by Eq. (2) we need to know (a) atomic positions  $\mathbf{R}_{\alpha,m}$ , (b) the atomic pseudopotentials  $v_{\alpha}$  for each atomic type  $\alpha$ , and (c) a method to solve Eq. (2). These issues are discussed next.

### A. Atomic structure

We postulate (rather than predict) a given profile of CM. This is done using a full three-dimensional atomistic model to describe the CM structures. We then express the strain energy of the system using the valence force field<sup>26</sup> (VFF) method. A conjugate gradient technique<sup>28</sup> is used to relax the atomic positions so that the strain energy is minimized. The local strain at each atomic site  $\mathcal{E}(\mathbf{R}_{\alpha,m})$  is calculated considering the distorted tetrahedron formed by the four nearest-neighbor atoms, as described in detail in Ref. 29.

### B. Atomic pseudopotentials

We construct empirical pseudopotentials that are fitted to reproduce, in addition to the bulk band structure at equilibrium, also effective masses, strained band offsets and the strain dependence of the band-edge energies (deformation potentials). We also fit ternary information, i.e., band-gap redshifts in  $(\text{AC})_1/(\text{BC})_1$  [111]-oriented SL (“CuPt” structure) and  $(\text{AC})_2/(\text{BC})_2$  [001]-oriented SL (“Z2” structure) with the respect to random alloy. The fit is accomplished by using a functional form for the pseudopotentials which is continuous in reciprocal space and *strain-dependent*:

$$v_{\alpha}(q, \mathcal{E}) = v_{\alpha}(q, 0) [1 + \delta v_{\alpha}(\mathcal{E}(\mathbf{R}_{\alpha,m}))], \quad (3)$$

where  $v_{\alpha}$  is the screened atomic pseudopotential and  $\mathcal{E}(\mathbf{R}_{\alpha,m})$  is the local strain tensor at atomic site  $\mathbf{R}_{\alpha,m}$ .

The strain dependence plays a crucial role for the CM applications. While it is possible to construct conventional<sup>30</sup> strain-independent pseudopotentials of type  $v_{\alpha}(q, 0)$  to give good band structure at equilibrium systems (e.g., bulk GaAs) and good band-gap deformation potentials  $a_{\text{gap}} = a_{\text{CBM}} - a_{\text{VBM}}$ , these pseudopotentials exhibit shortcomings when

the system is deformed with respect to the ideal structure. For example, the individual band-edge deformation potentials  $a_{\text{CBM}}$  and  $a_{\text{VBM}}$  and band offsets in lattice-mismatched systems are difficult to fit correctly even qualitatively. This is because the pseudopotential form  $v_\alpha(q,0)$  does not contain any dependence on the local atomic environment which would describe the change in the potential due to deformation. This shortcoming of  $v_\alpha(q,0)$  does not appear in self-consistently screened potentials since the latter builds in the effect of charge redistribution due to the deformation. The form  $v_\alpha(q,\mathcal{E})$  supplies this needed dependence of the potential on its atomic environment. For cubic materials, we model the pseudopotential dependence on  $\mathcal{E}$  by using the trace of the strain tensor  $[\text{Tr}(\mathcal{E})]$  to describe the changes in the local atomic environment. The functional form chosen for  $v_\alpha(q,0)$  is

$$v_\alpha(\mathbf{q},\mathcal{E}) = a_{0\alpha} \frac{(q^2 - a_{1\alpha})}{a_{2\alpha} e^{a_{3\alpha} q^2} - 1} [1 + a_{4\alpha} \text{Tr}(\mathcal{E})], \quad (4)$$

where  $a_{i\alpha}$   $i=0,1,2,3,4$  are the parameters to be fitted.

The functional form is chosen to give sufficient flexibility to describe as many physical quantities as possible without ‘‘overfitting’’ the potential by including too many parameters. It also provides a functional form that resembles the final form from the outset and will therefore only require some small optimization for each atomic type rather than dramatic changes, thus stabilizing the optimization process.

These types of pseudopotentials have been shown to produce reliable results for lattice-mismatched III-V systems where the strain dependence plays a crucial role: random alloys, strained superlattices, and embedded quantum dots.<sup>31,32</sup>

The pseudopotential fits and the parameters  $a_{i\alpha}$  employed in this study for GaAs, InAs, AlP, GaP, and InP are listed in the Appendix. A 5 Ry kinetic-energy cutoff was used when generating the pseudopotentials. To avoid discontinuities in the calculated band structure, a smoothing function was applied near the cutoff energy  $E_{\text{cut}}$ .<sup>33</sup> The Appendix compares the EPM calculated band-edge energies at high symmetry points, electron and heavy-hole effective masses, hydrostatic and biaxial deformation potentials with the first-principles and experimental values used as a reference in the fitting procedure. The Appendix further shows the natural and strained valence band offsets given by the applied pseudopotentials and makes comparison with the reference values. The Appendix also gives the band-gap redshifts in CuPt ([111]-oriented SL with period  $n=1$ ) and Z2 ([001]-oriented SL with period  $n=2$ ) alloy structures with respect to random alloy. In general, we see that the generated pseudopotentials reproduce well the reference values.

In the alloy environment we have used a weighted average for the anion pseudopotentials based on the local atomic configuration surrounding an anion site. For example, in  $\text{Ga}_{1-x}\text{In}_x\text{As}$ , there are two pseudopotentials  $v_{\text{As}(\text{Ga})}$  and  $v_{\text{As}(\text{In})}$  resulting from the fits performed for binary GaAs and InAs. The pseudopotential used at an As atomic site is

$$v_{\text{As}} = \frac{n_{\text{Ga}}}{4} v_{\text{As}(\text{Ga})} + \frac{n_{\text{In}}}{4} v_{\text{As}(\text{In})}, \quad (5)$$

where  $n_{\text{Ga}(\text{In})}$  denote how many of the four nearest-neighbor cations surrounding the As site are Ga (In) atoms, respectively. We emphasize that, although this weighted average of pseudopotentials in the *anion* sublattice *locally* resembles the spirit of virtual crystal approximation (VCA), the description of the full alloy (mixed *cation* sublattice) is based on explicit treatment of individual atoms rather than VCA.

In order to check the effect of spin-orbit (SO) splitting in the CM systems, we have constructed a set of pseudopotentials for GaAs and InAs including the SO effects. We use the same functional form as in Eq. (3), and include the SO interaction by introducing a nonlocal term.<sup>33</sup> This nonlocal potential is represented by a Kleinman-Bylander separable form in real space, which allows order- $N$  scaling for calculations with large system size.<sup>32</sup> The resulting pseudopotentials are listed in the Appendix which also compares the SO pseudopotential (SO-EPM) with the pseudopotential omitting SO effects (NSO-EPM), and the reference experimental and first-principles values. The accuracy of the SO-EPM can be seen to be similar to the NSO-EPM.

### C. Solving the Schrödinger equation

The realistic modeling of a CM system requires the use of supercells containing typically  $\sim 30\,000$  atoms. This sets special requirements for solving the electronic structure.

To expand the electronic wave functions, we use the plane-wave basis:

$$\psi_i = \sum_{\mathbf{G}} c_{\mathbf{k}+\mathbf{G}} e^{i\mathbf{k}+\mathbf{G}\cdot\mathbf{r}}, \quad (6)$$

where  $\mathbf{G}$  runs over the reciprocal lattice vectors fulfilling the kinetic-energy cutoff ( $\frac{1}{2}|\mathbf{k}+\mathbf{G}|^2 < 5\text{ Ry}$ ). Using this expansion for wave functions we calculate the eigenstates of the Schrödinger equation [Eq. (2)] using the folded spectrum method (FSM),<sup>34</sup> where one solves

$$(H - \epsilon_{\text{ref}})^2 \psi_i = (\epsilon_i - \epsilon_{\text{ref}})^2 \psi_i, \quad (7)$$

which gives identical solutions with Eq. (2). The crucial advantage of FSM is that we are able to solve a selected number of eigenstates around the reference energy  $\epsilon_{\text{ref}}$  without the need to solve all eigenstates of the Hamiltonian. For example, by choosing  $\epsilon_{\text{ref}}$  inside the band-gap we are able to resolve the band edge states which are of primary interest for the present application. Using this approach, the computational cost scales linearly as a function of the system size, allowing calculations with the required large system sizes, in contrast with conventional methods which scale as  $N^3$  ( $N$  corresponding to the number of atoms in the system) thus restricting  $N$  to  $\ll 10^3$  atoms.

## III. LATERAL COMPOSITION MODULATION WITHOUT SUPERLATTICE: GaAs/InAs

We first discuss the consequences of pure lateral CM, without the vertical SL. We take  $\text{Ga}_{0.5}\text{In}_{0.5}\text{As}$  as an example to illustrate the essential physical phenomena related to CM.

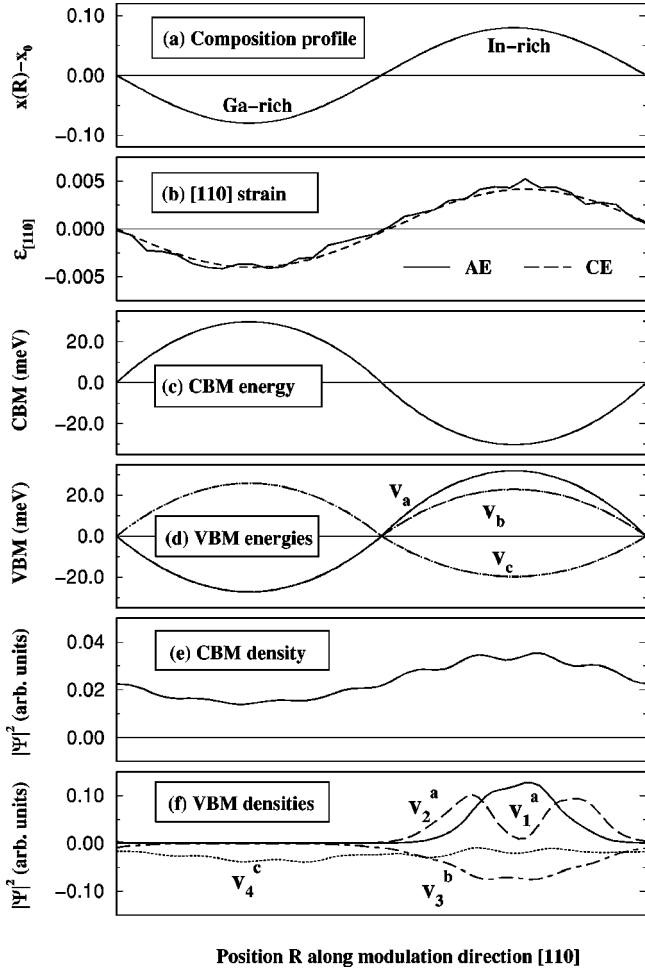


FIG. 3. The pure [110] composition modulation in  $\text{Ga}_{1-x}\text{In}_x\text{As}$ : (a) the sinusoidal composition profile; (b) the [110] strain calculated using the atomistic VFF method and using continuum elasticity; (c) the modeled CBM energy along the composition wave; (d) the modeled VBM energies along the composition wave; (e) the wave function squared for the lowest conduction band state; and (f) the wave function squared for the three highest valence band states. In (f),  $V_3$  and  $V_4$  are inverted for clarity.

### A. Construction of the composition modulation supercell

We first consider sinusoidal composition modulation in  $\text{Ga}_{1-x}\text{In}_x\text{As}$  at  $x_0=0.5$  and  $\vec{u}$  along a [110] direction using Eq. (1). We construct a periodic ‘‘supercell’’ containing a full period of  $x(R)$  of Eq. (1) by stacking along the  $\vec{u}$  direction  $n$  planes with lattice vectors perpendicular to the modulation  $a_1=N(\bar{1},1,0)a_0$ , and  $a_2=N(0,0,1)a_0$ , where  $a_0$  is the cubic lattice constant of  $\text{Ga}_{0.5}\text{In}_{0.5}\text{As}$  and  $N$  is an integer driving the lengths of the in-plane lattice vectors. For  $N=10$ , we have 200 cations and 200 anions per plane. The number of planes is  $n \approx (4/\sqrt{2})(\lambda/a_0)$ . For example, for  $\lambda=150 \text{ \AA}$  we have  $n=72$ , leading to a number of atoms (anions and cations) in the supercell of  $4N^2n=28\,800$ . In each plane we occupy the  $2N^2$  cation-lattice sites randomly<sup>35</sup>, so as to produce a plane composition given by  $x(R)$ . Figure 3(a) shows our composition profile  $x(R)$  along the  $\vec{u}=[110]$  direction with modulation amplitude  $A=8\%$ .

TABLE I. The elastic constants given by the applied valence force field for GaAs and InAs. Experimental values are also given as reference.

Material	$10^{11}\text{dyne/cm}^{-1}$		
	$C_{11}$	$C_{12}$	$C_{44}$
GaAs	12.03	5.70	5.20
GaAs(experimental)	12.11	5.48	6.04
InAs	8.53	4.90	3.14
InAs(experimental)	8.329	4.526	3.959

### B. Atomic relaxation and strain fields

Having constructed a periodic composition wave, we now permit all atoms in the supercell to relax away from their nominal zinc-blende sites so as to minimize the elastic VFF strain energy. No symmetry constraints are assumed, i.e., the atomic relaxation is not restricted to the modulation direction. We find that the main relaxation occurs in the [110] CM direction in the supercell: for the (110) planes in the Ga-rich (In-rich) region the interplanar spacing contracts (expands). To illustrate this, Fig. 3(b) shows the [110] strain component induced by pure CM. We note that the strain wave [Fig. 3(b)] is commensurate with the composition wave [Fig. 3(a)]. The solid line in Fig. 3(b) corresponds to the strain calculated directly using the VFF method, i.e., atomic elasticity. This strain is used throughout this work. The strain along the [110] direction is calculated by averaging over the atomic local strains in each (110) plane. The dashed line in the same figure shows the [110] strain calculated using continuum elasticity. Assuming the cartesian coordinate system  $x$ ,  $y$  and  $z$  corresponding to [100], [010] and [001] directions, the continuum elasticity tetragonal strain along the [110] direction can be evaluated as<sup>22</sup>

$$\mathcal{E}_{[110]} = \mathcal{E}_{xx} + \mathcal{E}_{yy} = \mathcal{E}_{zz} \frac{2c_{44} - c_{11} - 3c_{12}}{2c_{44} + c_{11} + c_{12}}, \quad (8)$$

$$\mathcal{E}_{zz} = \frac{a(x_0) - a(x)}{a(x)},$$

where  $c_{11}$ ,  $c_{12}$ , and  $c_{44}$  are elastic constants of a zinc-blende material, and  $a(x_0)$  and  $a(x)$  correspond to the lattice constant of  $\text{Ga}_{1-x}\text{In}_x\text{As}$  ( $x_0=0.5$ ). To make a consistent comparison between the strains calculated based on atomic and continuum elasticity, we have used the values for elastic constants directly derived from the VFF force constants listed for GaAs and InAs in Table I.<sup>29</sup> Comparison of the [110] strains in Fig. 3(b) reveals that atomic and continuum elasticity give very similar strain profiles and magnitudes [the small fluctuations in the atomic elasticity strain are due to averaging over randomly occupied (110) planes with finite size]. We will see in Fig. 7 below how this situation changes dramatically for individual layers in CM+SL systems.

### C. Simple model for band-edge energies and band alignment

In Sec. III D we will describe the results obtained by directly solving Eq. (2) for the minimum strain atomic configuration in Figs. 3 (a) and 3(b). Before presenting the results of the full calculation, it is instructive to consider in this

subsection how coupling of the strain with the composition wave is going to modify the energy levels relative to the random alloy. To study the *qualitative* physics we wish to consider the CBM and VBM energies along the [110] CM composition wave. In order to simply mimic the local atomic environment along the composition wave, we construct smaller [110]-oriented supercells.<sup>36</sup> We occupy the cation sublattice randomly in these cells so that the composition corresponds to  $x(\vec{R})$ . To imitate the average strain along the [110] direction in the large CM supercell [Fig. 3(b)], the shape of the small supercell is chosen in the following way: The supercell vector lengths along  $[\bar{1}10]$  and  $[001]$  correspond to the lattice constant of the  $x=0.50$  alloy given by Vegard's rule, while the length of the  $[110]$  cell vector is adjusted for each  $x(\vec{R})$  to give the strain along [110] illustrated in Fig. 3(b). Full relaxation of the atoms in the small supercell is then performed using the VFF method, and the eigenstates of the Hamiltonian (without spin-orbit interaction) are consequently solved using the same method (atomic pseudopotentials, folded-spectrum method) as used for the large CM cell as reported in our full numerical calculation in Sec. III D.

The resulting band-edge energies are shown in Figs. 3(c) and 3(d). Figure 3(c) shows that the modeled CBM energy goes up relative to the random alloy in the Ga-rich region and dips down in the In-rich region. The behavior of the three uppermost valence states is shown in Fig. 3(d). We label them  $V_a$ ,  $V_b$ , and  $V_c$  in order of the energies in the In-rich region. Analysis of the symmetry of these states reveals that they have  $[\bar{1}10]$  (heavy-hole),  $[001]$  and  $[110]$  (light-hole) character, respectively. We see that the energies of  $V_a$  and  $V_b$  are pushed up (down) in the In-rich (Ga-rich) region, while  $V_c$  behaves in an opposite way. It is interesting to note that in the In-rich region where  $\mathcal{E}_{[110]} > 0$  [Fig. 3(b)] there is a 10 meV splitting between  $V_a$  and  $V_b$ , while in the Ga-rich region where  $\mathcal{E}_{[110]} < 0$ , this splitting is almost zero. This important nonlinearity cannot be represented by the linear strain model used in the  $\mathbf{k}\cdot\mathbf{p}$  method.<sup>8,7,22</sup> This nonlinearity is responsible for the fact that  $V_a$  in the In-rich region is slightly above  $V_c$  in the Ga-rich region, indicating type-I band alignment (electrons and holes localized in the same spatial region). This effect was missed in Refs. 8, 7 and 22.

Figures 3(e) and 3(f) show the wave functions squared for the lowest conduction state and the four uppermost valence states as calculated in the full 28 800 atom CM system (no spin-orbit interaction). Indeed, the CBM and  $V_1$  are both localized in the In-rich region confirming the expected type-I band alignment for the studied band edges in Figs. 3(c) and 3(d). The superscripts in the valence band (VB) state labels in Fig. 3(f) refer to the three types of states ( $a, b, c$ ) identified in Fig. 3(d):  $V_1^a$  and  $V_2^a$  are the highest VB states both exhibiting  $a$ -type character, but  $V_2^a$  resides lower in energy due to an additional node in its wave function (seen as the double peaked structure in wave function squared).  $V_3$  exhibits only one maximum and is localized in the In-rich region and is thus assigned to be of type  $b$ . Finally,  $V_4$  is localized in the Ga-rich region and has to belong to type  $c$  based on Fig. 3(d). Since  $V_1^a$ ,  $V_2^a$ , and  $V_3^a$  have heavy-hole

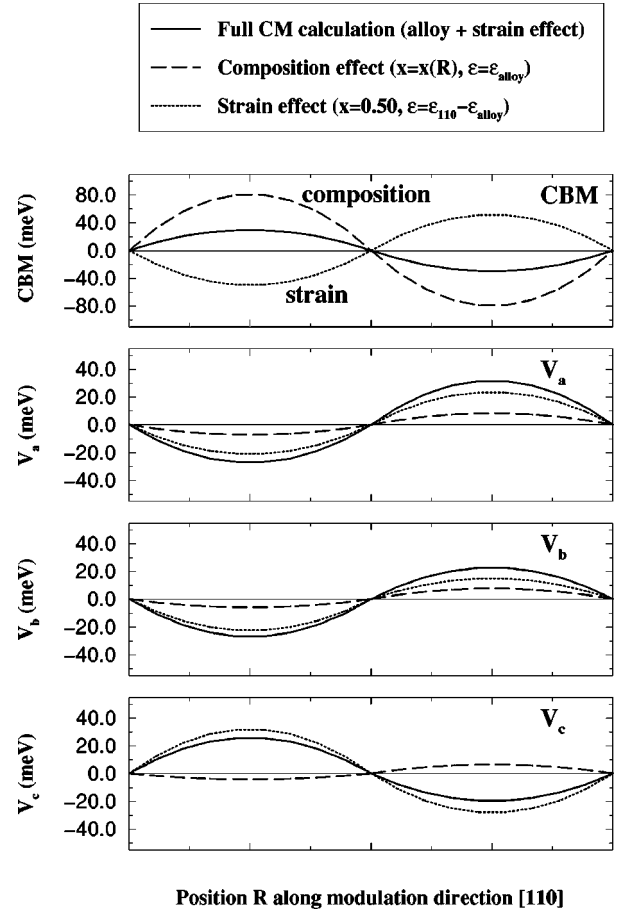


FIG. 4. The pure [110] composition modulation in  $\text{Ga}_{1-x}\text{In}_x\text{As}$ : the alloy and strain contributions to the modeled CBM and VBM energies along the composition wave.

character, their wave functions are more localized than the  $V_4$  light-hole state (which has a smaller effective mass along the [110] direction).

The physical effects leading to the composition dependence of the band-edge states  $\epsilon_{\text{VBM}}(x)$  and  $\epsilon_{\text{CBM}}(x)$  in Figs. 3(c) and 3(d) are analyzed in more detail in Fig. 4. We have separated the contributions originating from the composition change (“composition effect,” long dashed line) and the strain wave (“strain effect,” dotted line). The solid lines in Fig. 4 correspond to the combined effect [shown also in Figs. 3(c) and 3(d)]. To model the composition effect, the composition of the small 400 atom cell was adjusted to follow the composition wave  $x(\vec{R})$  and the volume of the cell was chosen accordingly (Vegard's rule). After this, a full atomic relaxation was performed resulting in strain denoted by  $\mathcal{E}_{\text{alloy}}$ . To model the strain effect the cell composition was kept fixed at  $x=x_0=0.50$ , but the cell geometry was adjusted to mimic the relaxation in the [110] direction due to CM wave; the volume change due to Vegard's rule was subtracted so that the sum of the alloy effect and strain effect calculations would correspond to the composition and cell shape in the full calculation. After assigning the composition and cell shape, a full atomic relaxation was performed. The resulting strain is denoted by  $\mathcal{E}=\mathcal{E}_{110}-\mathcal{E}_{\text{alloy}}$ .

We see from Fig. 4 that the composition effect shifts the CBM energy up (down) in the Ga-rich (In-rich) region, while all the energies of the three valence states are pushed down

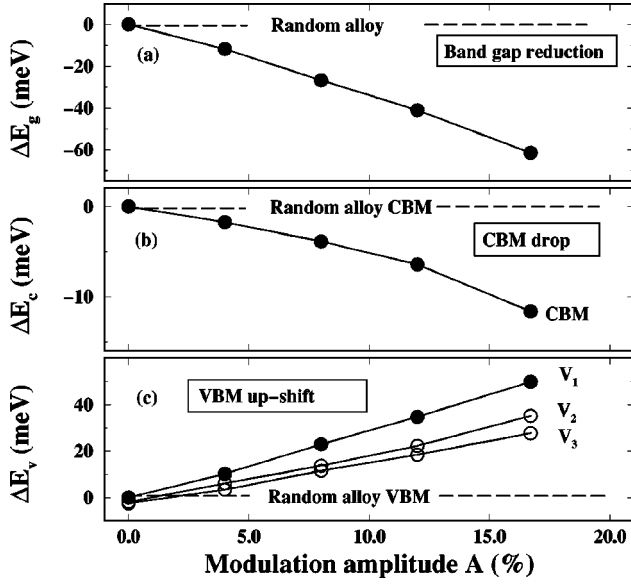


FIG. 5. The behavior of the band-gap and the band-edge states in  $\text{Ga}_{1-x}\text{In}_x\text{As}$  as a function of sinusoidal composition modulation amplitude  $A$ . The modulation wavelength  $\lambda$  is  $149 \text{ \AA}$ . The behavior of the lowest conduction band and the three uppermost valence band states are given relative to the random alloy (composition modulation with zero amplitude). In the composition modulated system the band gap experiences a significant narrowing (redshift).

(up). Thus, the band gap widens (narrows) in the Ga-rich (In-rich) region, as expected from the larger band gap for GaAs than for InAs. The strain effect has qualitatively the same contribution as the alloy effect for CBM and the two uppermost valence states. For the third valence state ( $V_c$ ), however, the strain has an opposite effect: due to strain  $V_c$  has its maximum in the Ga-rich region while  $V_a$  and  $V_b$  have their maxima in the In-rich region. Based on this decomposition analysis into alloy and strain contributions it is evident that an accurate description of both compositional and strain effects is essential for a realistic modeling of the band-edge states in a CM system.

#### D. Band-gap redshift

As the modeled band edges show in Figs. 3(c) and 3(d), the smallest band gap occurs in the In-rich region of the CM system. Combined with the information that the CBM and VBM are localized in the In-rich region [Figs. 3(e) and 3(f)] the CM is expected to induce band-gap narrowing (redshift) with respect to a random alloy. While Figs. 3(c) and 3(d) were the result of a simple model (Sec. III C), we now use direct diagonalization to solve Eq. (2) for the full 28 800 atom minimum strain configuration. The result is given in Fig. 5 which shows the behavior of CBM and uppermost VB states as a function of the CM amplitude  $A$  ( $A=0$  corresponds to a fully random system). We indeed see that CM shifts VBM up while CBM drops, the combined effect being a band-gap redshift which is about 40 meV for 10% modulation amplitude.

We have also made calculations where the composition profile  $f$  is changed from a sinusoidal to a steplike function. We see that the band-gap redshift increases slightly, for  $A=8\%$  the increase is  $\sim 5$  meV. Also, we have investigated

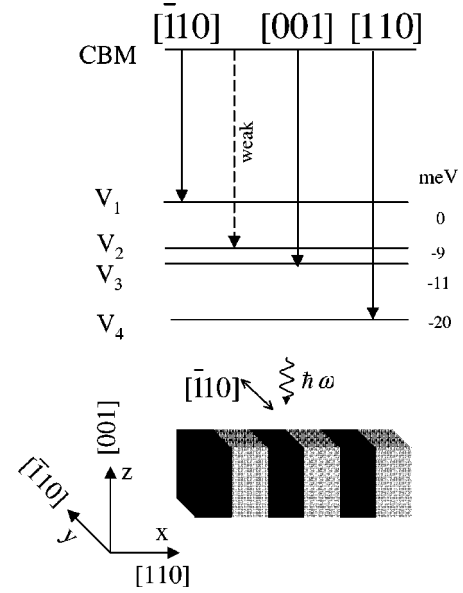


FIG. 6. Polarization of the lowest energy transitions for pure  $[110]$  composition modulation in  $\text{Ga}_{1-x}\text{In}_x\text{As}$  with  $\lambda=149 \text{ \AA}$  and  $A=8\%$ .

the effect of varying the modulation wavelength  $\lambda$ . We find that the behavior of the band-edge states and band gap is rather insensitive to  $\lambda$ : the band gap increases linearly by  $\sim 5$  meV when  $\lambda$  is varied from  $116 \text{ \AA}$  to  $182 \text{ \AA}$ .

#### E. Polarization of optical transitions

In order to analyze the polarization of the lowest energy optical transitions, we have calculated the dipole matrix elements between the lowest conduction state and the valence states

$$p_\alpha(i) = |\langle \psi_{\text{CBM}} | \mathbf{p}_\alpha | \psi_{V_i} \rangle|, \quad (9)$$

where  $i$  indexes the four highest valence states  $V_1$ ,  $V_2$ ,  $V_3$ , and  $V_4$ ; and  $\alpha$  denotes the cartesian components  $x$ ,  $y$ , and  $z$ . Since the CM is assumed along  $[110]$ , the interesting oscillator strengths to be determined are  $p_{[110]}$ ,  $p_{[\bar{1}10]}$ , and  $p_{[001]}$ . Based on the calculated cartesian matrix elements these can be expressed as

$$p_{[110]} = p_x + p_y,$$

$$p_{[\bar{1}10]} = -p_x + p_y, \quad (10)$$

$$p_{[001]} = p_z.$$

The full transition probability  $|p|^2$  is obtained as  $p_x^2 + p_y^2 + p_z^2$ .

Figure 6(a) shows the calculated polarizations. The lowest energy transition from CBM to  $V_1$  is found to be polarized along  $[\bar{1}10]$ , i.e., perpendicular to the CM wave. The transition probability for CBM to  $V_2$  is very small (weak transi-

tion). The transition from CBM to  $V_3$  is  $[001]$  polarized while the transition from CBM to  $V_4$  is  $[110]$  polarized.

#### IV. COMBINATION OF LATERAL COMPOSITION MODULATION AND VERTICAL SHORT-PERIOD SUPERLATTICE

Having illustrated the physics induced by a pure lateral CM in Sec. III, we now turn to modeling the combined system of lateral CM and vertical SL which corresponds to the actual experimental case.

##### A. Structure: Integer vs. fractional period superlattice GaAs/InAs

Experimental studies<sup>9,11–13</sup> show that the strongest lateral CM is observed when superlattice layers have *noninteger* values, i.e., for  $(AC)_n/(BC)_m$  superlattice ( $n, m \neq 1, 2, \dots$ ). To gain insight into the role of the superlattice period, we investigate the two structures illustrated in Figs. 1 and 2. The atomic positions shown correspond to minimum strain configuration, the atomic strain being calculated as described in Sec. II A. The crucial difference between Figs. 1 and 2 is the superlattice period: Fig. 1(b) shows *integer* ( $n=2$ ) period superlattice while in Fig. 2(b) the superlattice period is *fractional*  $n=1.5$ . In the integer period superlattice, pure binary monolayers follow each other, while in the fractional period superlattice an alloy monolayer of  $\text{In}_x\text{Ga}_{1-x}\text{As}$  is sandwiched between the pure binary layers. It is evident that both the illustrated structures represent an ideal model of the actual experimentally grown structures [e.g.  $(\text{AlAs})_{1.44}/(\text{InAs})_{1.56}$  (Ref. 11)]. We further note that the experimental CM+SL structures commonly exhibit cusplike behavior of the superlattice layers. In our model this phenomenon is neglected at present, and we concentrate on providing understanding for the principal physics related to the illustrated model structures.

##### B. Atomic relaxation and strain fields in GaAs/InAs

Figure 7 shows the atomic relaxation in the case of  $[110]$  CM on which we superimpose a  $[001]$  GaAs/InAs SL with period  $n=1.5$ . Panel (a) compares the average (in the vertical  $[001]$  direction)  $[001]$  and  $[110]$  strains in CM+SL (solid lines) and pure CM (filled and open circles) systems. Rather surprisingly, we see that the *average* strains are nearly identical in pure CM and in CM+SL systems. Thus, the addition of fractional period superlattice bears little influence on the *average* strain which is determined by the average composition along the CM direction. In contrast, panels (b) and (c) show that the  $[001]$  and  $[110]$  strains calculated for *individual atomic layers* have large deviations from the average behavior. The first and second layers [labeling of the atomic layers is shown in Fig. 2(c)] exhibit qualitatively similar strain profiles with the average strain shown in panel (a), while the third layer shows an opposite behavior. These strain profiles are a consequence of the  $[001]$ -oriented buckling of the atomic layers<sup>23</sup> which cannot be described by continuum models.<sup>8,7,22</sup>

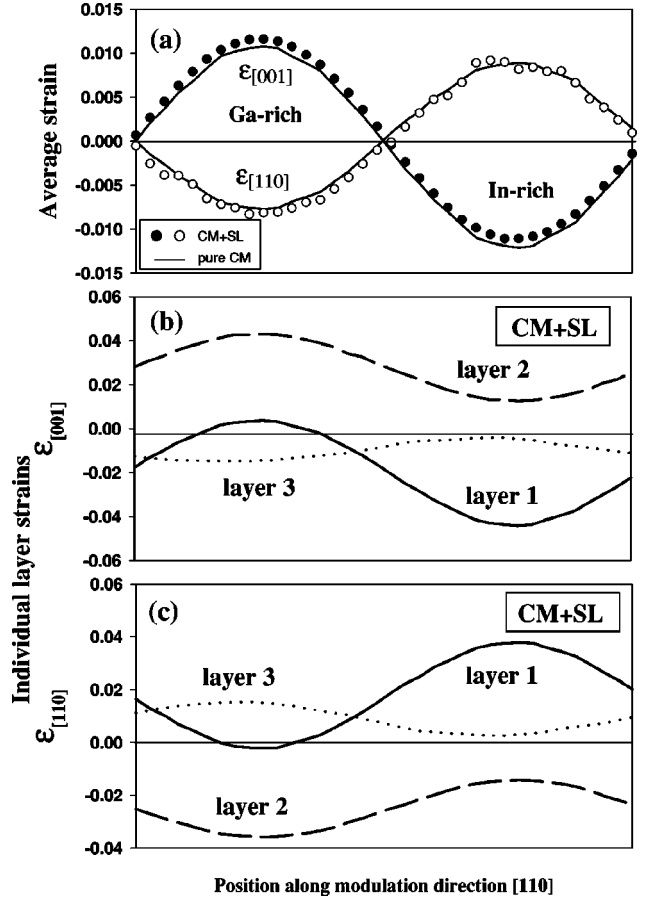


FIG. 7. Comparison of strain between the relaxed pure  $[110]$  composition modulation and combined  $[110]$  composition modulation +  $[001]$  vertical superlattice systems. The modeled systems correspond to  $\text{Ga}_{1-x}\text{In}_x\text{As}$  with  $A=16.7\%$ ,  $\lambda=149 \text{ \AA}$ . The vertical superlattice has a fractional period ( $n=1.5$ ). While (a) shows that *vertically averaged*  $[110]$  and  $[001]$  strains are nearly identical in pure CM and CM+SL systems, (b) and (c) show that the strains calculated for individual layers in the CM+SL structure deviate considerably from the average behavior. The labeling of atomic layers is shown in Fig. 2 (c).

##### C. Wave function localization and band alignment: GaAs/InAs, GaP/InP, and AlP/GaP

In Fig. 8 we compare the wave function squared in three CM+SL systems: panel (a) corresponds to  $\text{Ga}_{1-x}\text{In}_x\text{As}$  as calculated without the spin-orbit interaction, panel (b) shows the result for the same  $\text{Ga}_{1-x}\text{In}_x\text{As}$  system but including the spin-orbit effects, and panel (c) shows the wave functions squared in  $\text{Ga}_{1-x}\text{In}_x\text{P}$ .

Comparison between Fig. 3 (showing wave function densities for pure CM systems) and Fig. 8(a) showing the wave function densities in CM+SL system, reveals that the type-I band alignment exhibited in the pure CM system is preserved in the CM+SL system. We further note the close similarity between the CM and CM+SL systems in the CBM and the two uppermost valence states, suggesting that the character of the band-edge states is mainly determined by the CM wave rather than the SL. However, the effect of SL becomes evident with the deeper valence states which have a different character from the pure CM system as described in detail below (Sec. IV E).

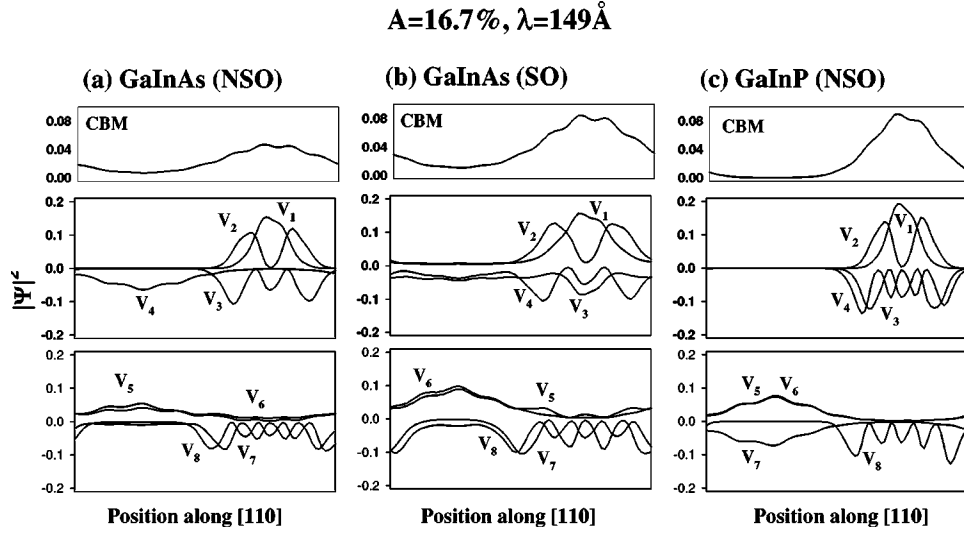


FIG. 8. The wave function squared for the lowest conduction band state and the eight highest valence band states in  $\text{Ga}_{1-x}\text{In}_x\text{As}$  and  $\text{Ga}_{1-x}\text{In}_x\text{P}$  [110] CM +  $n=1.5$  [001] SL systems. For  $\text{Ga}_{1-x}\text{In}_x\text{As}$ , comparison between the calculations excluding (NSO) (a) and including (SO) (b) spin-orbit splitting is made.  $V_3$ ,  $V_4$ ,  $V_7$ , and  $V_8$  are inverted for clarity.

The main effect of the spin-orbit interaction in the binary GaAs or InAs system is that it splits the otherwise triply degenerate VBM  $\Gamma_{15v}$  into two components: doubly degenerate  $\Gamma_{8v}$ , and a split-off state  $\Gamma_{7v}$ , 0.34 (0.38) eV lower in energy in GaAs (InAs). The question we want to ask is: does this affect the delicate VBM structure in CM+SL structure and if so, how? Comparison between panels (a) and (b) of Fig. 8 corresponding to calculations excluding and including the spin-orbit effects reveals only minor differences: the CBM and the two uppermost valence states exhibit the same character, while small differences are visible in the order of the lower valence band states. We thus conclude that, surprisingly, the spin-orbit interaction does not play a dominant role in determining the behavior of the band-edge states in the CM+SL systems.

The wave function densities shown for the  $\text{Ga}_{1-x}\text{In}_x\text{P}$  CM+SL system in Fig. 8(c) show that  $\text{Ga}_{1-x}\text{In}_x\text{P}$  also exhibits type-I band alignment. In Fig. 9 we use  $\text{Al}_x\text{Ga}_{1-x}\text{P}$  as

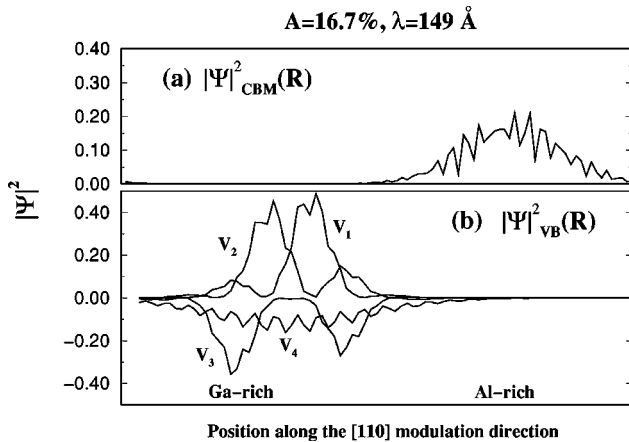


FIG. 9. The wave function squared for the lowest conduction band state and the three highest valence band states in  $\text{Al}_x\text{Ga}_{1-x}\text{P}$  [110] CM +  $n=1.5$  [001] SL system demonstrating a type-II band alignment.  $V_3$  and  $V_4$  are inverted for clarity.

an example to demonstrate type-II band alignment in the [110] CM + [001] SL ( $n=1.5$ ) system. It is immediately evident that CBM and VBM wave functions are localized in different regions. This is a direct consequence of the type-II natural (unstrained) band offset between AlP and GaP: the VBM (CBM) of GaP resides 0.54 (0.58) eV lower than in AlP. Thus, it is possible to generate a type-II CM if one uses constituents that already have a type-II alignment. This phenomenon could be used, e.g., in reducing the electron-hole recombination in a solar-cell structure as proposed by Mascarenhas *et al.*<sup>27</sup> However,  $\text{Al}_x\text{Ga}_{1-x}\text{P}$  alloy seems not to be a good candidate for this application due to inefficient light absorption induced by the indirect band gap (see Sec. IV E).

#### D. Band-gap redshift: GaAs/InAs, AlAs/InAs, GaP/InP

Figure 10 shows the behavior of the band edges and band gap as a function of the modulation amplitude  $A$  for the combined [110] CM and [001] SL ( $n=1.5$ ) structure. Panel (a) also shows the band-gap reduction for the system with [110] CM + [001]  $n=2.0$  SL and pure [110] CM. The data points at  $A=0.0$  correspond to pure SL without CM. We see that the pure [001] SL induces a significant redshift which mainly originates from downshift in CBM. The contribution to the redshift from fractional ( $n=1.5$ ) and integer ( $n=2$ ) period superlattices is nearly the same. Panel (a) reveals also that the redshift induced by the CM+SL system is nearly a linear combination of the pure CM and SL contributions.

Figure 11 compares the shift in the band-edge states and band gap between the  $\text{Ga}_{1-x}\text{In}_x\text{As}$  and  $\text{Ga}_{1-x}\text{In}_x\text{P}$  CM+SL systems. We see that the CM+SL induced band-gap redshift is much larger in  $\text{Ga}_{1-x}\text{In}_x\text{P}$  than in  $\text{Ga}_{1-x}\text{In}_x\text{As}$ . This is induced by two factors: (a) the redshift for pure  $n=1.5$  SL ( $A=0$ ) is considerably larger for  $\text{Ga}_{1-x}\text{In}_x\text{P}$  than for  $\text{Ga}_{1-x}\text{In}_x\text{As}$  and (b) the redshift induced by CM is larger in  $\text{Ga}_{1-x}\text{In}_x\text{P}$  than in  $\text{Ga}_{1-x}\text{In}_x\text{As}$  as can be seen by comparing the slopes in Fig. 11(a). These effects are a consequence of the

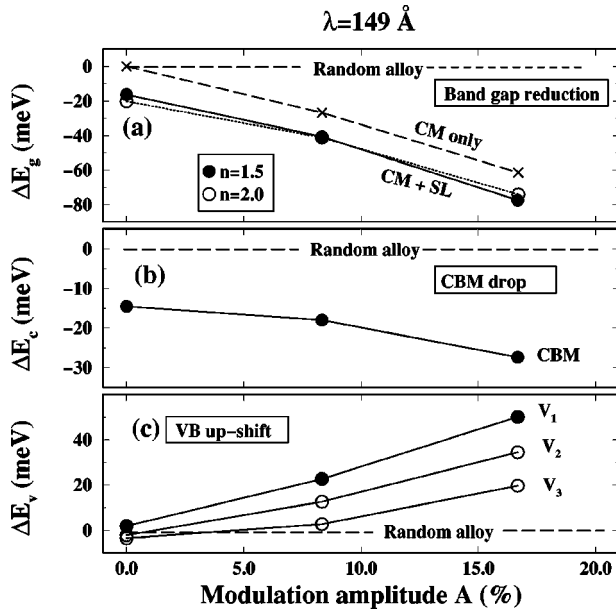


FIG. 10. The behavior of the band-gap and the band-edge states in a  $\text{Ga}_{1-x}\text{In}_x\text{As}$  system exhibiting both [110] composition modulation and [001] superlattice ( $n=1.5$ ) as a function of sinusoidal composition modulation amplitude  $A$ . The modulation wavelength  $\lambda$  is 149 Å. In (a) the band-gap redshift is compared with  $\text{Ga}_{1-x}\text{In}_x\text{As}$  systems (i) exhibiting only composition modulation and (ii) composition modulation and integer period ( $n=2$ ) superlattice. Zero modulation amplitude  $A=0.0$  represents the effect of pure vertical superlattices. The lowest conduction band (b) and the three uppermost valence band states (c) are given relative to the random alloy (dashed horizontal lines).

band alignment between the binary materials: (i) the valence band offset between GaP and InP (0.11 eV) is about twice the value for GaAs/InAs (0.057 eV), (ii) the conduction band offset, calculated at  $\Gamma$  point which is relevant for the alloy comparison, is significantly larger (1.30 eV) for GaP/InP than for GaAs/InAs (1.04 eV). The conduction band offsets are thus much larger than valence band offsets; Fig. 11(b) reveals that the drop in the conduction band minimum indeed

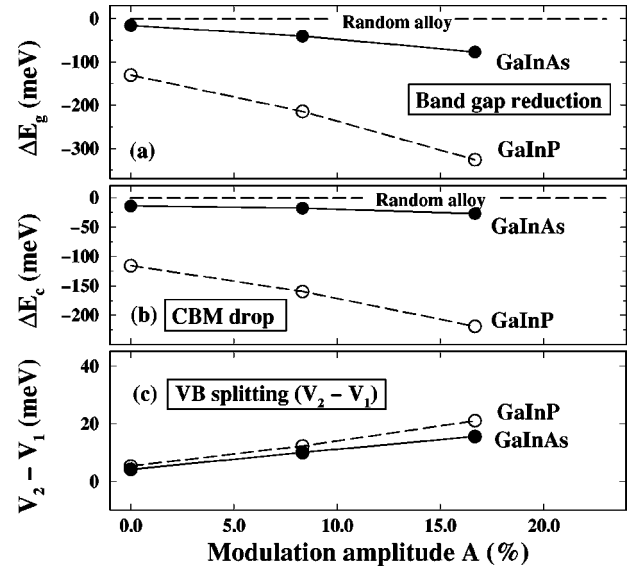


FIG. 11. The comparison of the band-gap and the band-edge states in  $\text{Ga}_{1-x}\text{In}_x\text{As}$  and  $\text{Ga}_{1-x}\text{In}_x\text{P}$  systems exhibiting both [110] composition modulation and [001] superlattice ( $n=1.5$ ) as a function of sinusoidal composition modulation amplitude  $A$ . The modulation wavelength  $\lambda$  is 149 Å for  $\text{Ga}_{1-x}\text{In}_x\text{As}$  and 144 Å for  $\text{Ga}_{1-x}\text{In}_x\text{P}$ . Zero modulation amplitude  $A=0.0$  represents the effect of pure vertical superlattices. The behavior of the band gap (a) and the lowest conduction band (b) are shown relative to the random alloy (dashed horizontal lines). The splitting between the two uppermost valence band states is shown in (c).

constitutes most of the band-gap redshift in both materials. Figure 11(c) shows that the energy difference between the two highest valence band states increases nearly linearly from a few meV to  $\sim 15$  meV as a function of modulation amplitude  $A$  in both  $\text{Ga}_{1-x}\text{In}_x\text{As}$  and  $\text{Ga}_{1-x}\text{In}_x\text{P}$ .

The calculated band-gap redshifts are in good agreement with available experimental data. In  $\text{Ga}_{1-x}\text{In}_x\text{As}$  the reported values are in the range from a few tens of meV up to  $\sim 100$ .<sup>11</sup> In  $\text{Ga}_{1-x}\text{In}_x\text{P}$  the reported values are typically significantly larger ( $\sim 250$  meV).<sup>5,6,8</sup>

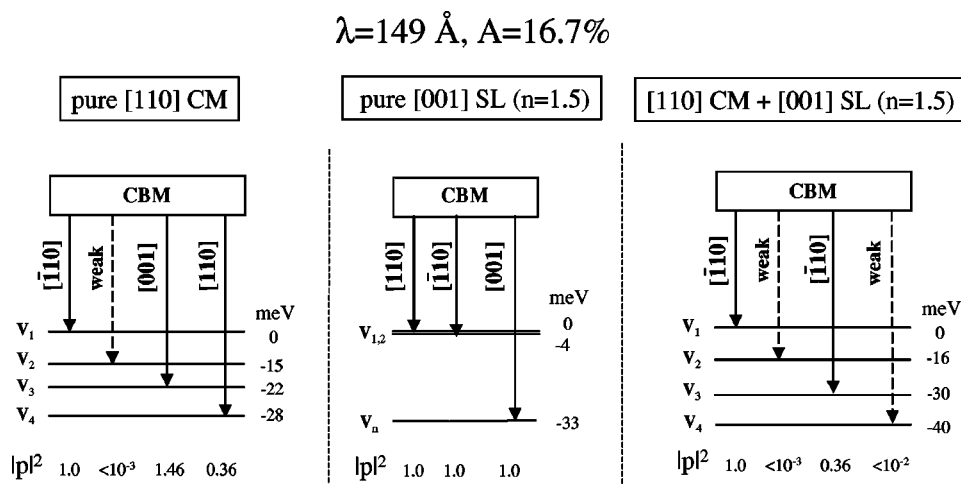


FIG. 12. Polarization of the lowest energy transitions in  $\text{Ga}_{1-x}\text{In}_x\text{As}$  for (i) pure [110] composition modulation, (ii) pure [001] fractional ( $n=1.5$ ) period superlattice, and (iii) [110] composition modulation + [001] fractional ( $n=1.5$ ) period superlattice.

TABLE II. The pseudopotential fit for GaAs.

Properties	SO-EPM	NSO-EPM	LAPW	Expt.
$\Gamma_{1c}$	1.52	1.51		1.52 <sup>a</sup>
$X_{5v}$	-2.13	-2.11		-2.96 <sup>b,c</sup>
$X_{1c}$	1.95	1.86		1.98 <sup>b,c</sup>
$L_{3v}$	-0.77	-0.84		-1.30 <sup>b,d</sup>
$L_{1c}$	1.75	1.78		1.81 <sup>b,c</sup>
$m_e$	0.092	0.087		0.067 <sup>e</sup>
$m_{hh}(100)$	0.47	0.47		0.40 <sup>f</sup>
$a_g(\Gamma)$	-8.63	-8.06	-7.25	-8.27 <sup>g</sup>
$a_v(\Gamma)$	-1.10	-0.99	-1.21	
$b$	-1.77	-1.52	-1.99	-1.7 <sup>h</sup>
$\Delta_0(\Gamma_{7v}-\Gamma_{8v})$	0.33	0.00		0.34 <sup>b</sup>
<sup>a</sup> Reference 37.		<sup>e</sup> Reference 41.		
<sup>b</sup> Reference 38.		<sup>f</sup> Reference 42.		
<sup>c</sup> Reference 39.		<sup>g</sup> Reference 43.		
<sup>d</sup> Reference 40.		<sup>h</sup> Reference 44.		

### E. Polarization of optical transitions

Figure 12 illustrates the polarizations calculated for the lowest energy transitions in pure [110] CM, pure [001] SL ( $n=1.5$ ), and [110] CM + [001] SL systems.

We find that the lateral CM and vertical SL act as sequential filters. (i) Similar to Fig. 6, in the pure [110] CM the band-to-band transition has  $[\bar{1}10]$  polarization. The next transition with a significant total probability is 22 meV higher in energy and [001] polarized. Among the four lowest energy transitions no [110] polarized transition is found. Thus, the effect of [110] modulation is to enhance  $[\bar{1}10]$  polarization perpendicular to the CM direction over the [110] polarization parallel to CM, but also to allow [001] polarized transition. (ii) For pure [001] SL ( $n=1.5$ ) the VBM is slightly ( $\sim 4$  meV) split due to random occupation of the

TABLE III. The pseudopotential fit for InAs.

Properties	SO-EPM	NSO-EPM	LAPW	Expt.
$\Gamma_{1c}$	0.41	0.42		0.42 <sup>a</sup>
$X_{5v}$	-1.88	-1.78		-2.4 <sup>b</sup>
$X_{1c}$	2.27	2.29		2.34 <sup>b,c</sup>
$L_{3v}$	-0.72	-0.71		-0.9 <sup>b</sup>
$L_{1c}$	1.41	1.43		1.71 <sup>b,c</sup>
$m_e$	0.032	0.028		0.023 <sup>d</sup>
$m_{hh}(100)$	0.48	0.53		0.35 <sup>e</sup>
$a_g(\Gamma)$	-5.33	-6.10	-4.88	-6.6 <sup>f</sup>
$a_v(\Gamma)$	-0.85	-1.01	-1.00	
$b$	-1.85	-1.70	-1.67	-1.8 <sup>f</sup>
$\Delta_0(\Gamma_{7v}-\Gamma_{8v})$	0.36	0.00		0.38 <sup>g</sup>
<sup>a</sup> Reference 45.		<sup>e</sup> Reference 48.		
<sup>b</sup> Reference 46.		<sup>f</sup> Reference 49.		
<sup>c</sup> Reference 47.		<sup>g</sup> Reference 50.		
<sup>d</sup> Reference 41.				

TABLE IV. The pseudopotential fit for AlP.

Properties	NSO-EPM	LAPW	Expt.
$\Gamma_{1c}$	4.73		4.38 <sup>a</sup>
$X_{5v}$	-2.42		-2.27 <sup>b</sup>
$X_{1c}$	2.27		2.51 <sup>c</sup>
$L_{3v}$	-0.98		-0.8 <sup>b</sup>
$L_{1c}$	3.61		3.57 <sup>d</sup>
$m_e$	0.26		0.21 <sup>e</sup>
$m_{hh}(100)$	0.62		0.51 <sup>f</sup>
$a_g(\Gamma)$	-7.46	-8.50	-9.3 <sup>g</sup>
$a_v(\Gamma)$	1.98	2.64	
$b$	-2.09	-1.59	-1.8 <sup>h</sup>
<sup>a</sup> Reference 51.		<sup>e</sup> Reference 54.	
<sup>b</sup> Reference 46.		<sup>f</sup> Reference 55.	
<sup>c</sup> Reference 52.		<sup>g</sup> Reference 44.	
<sup>d</sup> Reference 53.		<sup>h</sup> Reference 56.	

mixed layer. The two lowest energy transitions to  $V_1$  and  $V_2$  are [110] and  $[\bar{1}10]$  polarized. We also find a [001] polarized transition which, however, is 33 meV higher in energy. Thus, the pure [001] SL allows both  $[\bar{1}10]$  and [110] transitions but does not favor [001] polarization perpendicular to the superlattice layers. (iii) The [110] CM and [001] SL system combine the effects of the two underlying structures: either [001] or  $[\bar{1}10]$  polarizations are not included among the four lowest energy transitions, but  $[\bar{1}10]$  polarization, allowed by both pure structures, is dominating.

In experimental studies,<sup>6-8,11,13</sup> the polarization component perpendicular to the CM direction is commonly found to be clearly favored over the component parallel to the CM wave. Our computational results analyzed above are indeed in agreement with this observation. Furthermore, the transitions with perpendicular polarization have been observed to have a lower energy than the transitions with parallel polarization to the CM direction.<sup>6-8,11,13</sup> Our calculated results are also in agreement with this observation.

TABLE V. The pseudopotential fit for GaP.

Properties	NSO-EPM	LAPW	Expt.
$\Gamma_{1c}$	2.86		2.86 <sup>a</sup>
$X_{5v}$	-2.23		-2.7 <sup>b</sup>
$X_{1c}$	2.32		2.35 <sup>c</sup>
$L_{3v}$	-0.95		-1.2 <sup>b</sup>
$L_{1c}$	2.73		2.71 <sup>d</sup>
$m_e$	0.155		0.127 <sup>e</sup>
$m_{hh}(100)$	0.50		0.45 <sup>f</sup>
$a_g(\Gamma)$	-9.3	-7.99	-9.3 <sup>g</sup>
$a_v(\Gamma)$	-2.6	-0.58	
$b$	-2.45	-1.97	-1.8 <sup>h</sup>
<sup>a</sup> Reference 57.		<sup>e</sup> Reference 54.	
<sup>b</sup> Reference 46.		<sup>f</sup> Reference 55.	
<sup>c</sup> Reference 52.		<sup>g</sup> Reference 44.	
<sup>d</sup> Reference 53.		<sup>h</sup> Reference 56.	

TABLE VI. The pseudopotential fit for InP.

Properties	NSO-EPM	LAPW	Expt.
$\Gamma_{1c}$	1.45		1.46 <sup>a</sup>
$X_{5v}$	-1.95		-2.20 <sup>b</sup>
$X_{1c}$	2.25		2.38 <sup>a,c</sup>
$L_{3v}$	-0.78		-1.23 <sup>d</sup>
$L_{1c}$	1.94		2.03 <sup>e,a</sup>
$m_e$	0.088		0.077 <sup>f</sup>
$m_{hh}(100)$	0.46		0.56 <sup>g</sup>
$a_g(\Gamma)$	-6.84	-5.18	-6.4 <sup>h</sup>
$a_v(\Gamma)$	-0.49	-0.41	
$b$	-1.71	-1.97	-2.0 <sup>a</sup>

<sup>a</sup>Reference 58.<sup>c</sup>Reference 62.<sup>b</sup>Reference 59.<sup>f</sup>Reference 63.<sup>c</sup>Reference 60.<sup>g</sup>Reference 64.<sup>d</sup>Reference 61.<sup>h</sup>Reference 44.

We have also analyzed the transition probabilities for the  $\text{Al}_x\text{Ga}_{1-x}\text{P}$  CM+SL system exhibiting type-II band alignment (Fig. 9). The full transition probabilities from the CBM to the four uppermost valence states are extremely small due to the lack of spatial overlap in the conduction and valence band wave functions. Type-II band alignment is present also in reciprocal space: decomposition of the CBM into Bloch states with  $k$ -vector sampling in the principal directions in the first Brillouin zone, reveals that it has very little  $\Gamma$  character, while VBM is principally  $\Gamma$ -like. This is an obvious consequence of both AlP and GaP binaries having an indirect gaps in reciprocal space. In fact, we find that already the pure  $n=1.5$  SL is indirect system in reciprocal space.

TABLE VII. Calculated valence band offsets of AC/BC, strained on a substrate lattice constant  $a_{||}$  in the  $\{001\}$  plane. For the strained material (**boldfaces**) the lattice constant along the  $[001]$  direction ( $a_{\perp}$ ) is fully relaxed by using the valence force field approach.  $a^*$  denotes *natural* unstrained valence band offsets, i.e.,  $E_{\text{VBM}}^{\text{AC}}(a_{\text{AC}}) - E_{\text{VBM}}^{\text{BC}}(a_{\text{BC}})$ . A positive offset means that the VBM energy of the material AC in AC/BC is above that of BC.

AC/BC	$a_{  }$	LAPW offset (eV)	NSO-EPM offset (eV)	SO-EPM offset (eV)
InAs/GaAs	$a^*$	0.057	0.056	0.045
<b>InAs</b> /GaAs	$a_{\text{GaAs}}$	0.38	0.40	0.42
InAs/ <b>GaAs</b>	$a_{\text{InAs}}$	-0.25	-0.22	-0.39
GaP/AlP	$a^*$	0.54	0.54	
InAs/AlAs	$a^*$	0.58	0.56	
<b>InAs</b> /AlAs	$a_{\text{AlAs}}$	0.89	0.91	
InAs/ <b>AlAs</b>	$a_{\text{InAs}}$	0.13	0.13	
InP/GaP	$a^*$	0.11	0.09	
<b>InP</b> /GaP	$a_{\text{GaP}}$	0.43	0.43	
InP/ <b>GaP</b>	$a_{\text{InP}}$	-0.32	-0.25	

TABLE VIII. Calculated band-gap redshifts  $\Delta E_g$  with respect to random alloy in CuPt ( $[111]$ -oriented SL with period  $n=1$ ) and Z2 ( $[001]$ -oriented SL with period  $n=2$ ) structures.

		$\Delta E_g$ NSO-EPM (eV)	$\Delta E_g$ LAPW (eV)
GaAs/InAs	CuPt	-0.05	-0.25
	Z2	-0.02	-0.05
GaP/InP	CuPt	-0.34	-0.42
	Z2	-0.12	-0.11

## V. SUMMARY AND CONCLUSIONS

We apply (i) atomistic description for strain as calculated with a valence force field approach, (ii) specially constructed strain-dependent empirical pseudopotentials, and (iii) plane-wave basis for the expansion of electronic wave functions to resolve the atomic and electronic structure resulting from lateral composition modulation in vertical short-period superlattices. Detailed analysis of a pure CM wave in  $\text{Ga}_{1-x}\text{In}_x\text{As}$  alloy shows that a careful consideration of both strain and alloy composition effects are necessary for a realistic description of the CM system. This fact is emphasized in the combined CM+SL system where the orthogonal strain fields, induced by CM and SL composition waves with different characteristic lengths, interact in a complex manner.

We show that for GaAs/InAs and GaP/InP systems, the electron-hole localization in type-I, i.e., the natural band alignment between the binaries, persists in the CM+SL system. Similarly for AlP/GaP systems, exhibiting type-II alignment between the binary compounds, we find type-II alignment also in the CM+SL system. Both CM and SL are found to contribute significantly to the behavior of band-edge states in CM+SL system:

(i) Both CM and SL induce band-gap narrowing with respect to random alloy, the main contribution originating from a drop in conduction band energy. The GaP/InP system is found to exhibit significantly larger band-gap reduction than GaAs/InAs. This is a consequence of the larger natural conduction and valence band offsets between GaP and InP than between GaAs and InAs.

(ii) The symmetry of the uppermost valence band states is strongly influenced by both CM and SL. As a consequence, the lowest energy optical transitions between conduction and valence band exhibit polarization: the component perpendicular to the CM wave has the lowest energy and highest transition probability, and the component parallel to the CM wave is suppressed by a shift to higher energy. The strong polarization dependence is in agreement with experimental observations.

TABLE IX. Screened atomic pseudopotential parameters for the arsenide semiconductors *excluding* the spin-orbit interaction. The  $a$  parameters refer to Eq. (4). A 5 Ry cutoff was used in the fitting.

	$a_0$	$a_1$	$a_2$	$a_3$	$a_4$
Ga	55 738.5	2.793	3209.4	0.283	1.862
In	107.755	1.915	3.460	0.414	1.665
As(GaAs)	48.54	2.536	1.463	0.494	0.000
As(InAs)	49.614	2.737	1.523	0.574	0.000

TABLE X. Screened atomic pseudopotential parameters for the arsenide semiconductors *including* the spin-orbit interaction. The  $a$  parameters refer to Eq. (4). A 5 Ry cutoff was used in the fitting.

	$a_0$	$a_1$	$a_2$	$a_3$	$a_4$
Ga	123 090.0	2.270	3 210.125	0.625	1.630
In	202.622	1.883	5.052	0.488	1.336
As(GaAs)	12.301	2.885	1.151	0.261	0.000
As(InAs)	93.056	2.620	1.972	0.693	0.000

In AlP/GaP CM+SL systems the optical transition probabilities are small due to an indirect band gap, which makes the practical exploitation of the type-II band alignment difficult, e.g., in solar-cell applications.

In general, our results thus show that if the control in growth parameters to select desirable CM amplitude ( $A$ ) and wavelength ( $\lambda$ ) etc., was achieved, the optical properties of semiconductor alloys could be tailored.

#### ACKNOWLEDGMENTS

We thank S.-H. Wei for providing the LAPW values employed in pseudopotential fits. T. M. acknowledges the financial support by the Väisälä Foundation (Helsinki, Finland). This work was supported by the U.S. Department of Energy, OER-BES-DMS Grant No. DE-AC36-83-CH10093. The calculations were performed using the Cray T3E, located at the National Energy Research Scientific Computing Center which is supported by the Office of Energy Research of the U.S. Department of Energy.

TABLE XI. Screened atomic pseudopotential parameters for the phosphide semiconductors. The  $a$  parameters refer to Eq. (4). A 5 Ry cutoff was used in the fitting.

	$a_0$	$a_1$	$a_2$	$a_3$	$a_4$
Al	59.399	1.880	4.585	0.212	1.008
Ga	568.082	3.000	47.76	0.201	2.488
In	640.312	1.708	24.54	0.241	2.117
P(AlP)	17.148	2.454	1.147	0.282	0.000
P(GaP)	36.874	2.646	1.375	0.402	0.000
P(InP)	23.721	2.707	1.225	0.392	0.000

#### APPENDIX: DESCRIPTION OF EMPIRICAL PSEUDOPOTENTIALS

In this Appendix we describe the empirical pseudopotential fits applied in this study. We use the notation NSO-EPM (SO-EPM) for pseudopotentials omitting (including) spin-orbit effects. In Tables II–VI the pseudopotential fits (EPM) are compared with the experimental data<sup>37–64</sup> and first-principles calculations (LAPW). Illustrated are band energies at high symmetry points (eV with respect to  $\Gamma_{15v}$ ), the band-gap hydrostatic deformation potential  $a_g(\Gamma)$ , the valence band maximum hydrostatic deformation potential  $a_v(\Gamma)$ , biaxial deformation potential  $b$ , the electron effective mass  $m_e$ , and the heavy-hole effective mass ( $m_{hh}$ ).  $\Delta_0$  denotes the spin-orbit splitting value. Table VII gives the calculated natural and strained valence band offsets. Table VIII gives the band-gap redshifts in CuPt ([111]-oriented SL with period  $n=1$ ) and Z2 ([001]-oriented SL with period  $n=2$ ) with respect to random alloy. Tables IX–XI list the pseudopotential parameters resulting from the fits.

\*Electronic address: alex\_zunger@nrel.gov

- <sup>1</sup>A. Zunger and S. Mahajan, in *Handbook of Semiconductors*, (Elsevier, Amsterdam, 1994), Vol. 3B (see Sec. 4.3.1), p. 1399.
- <sup>2</sup>A.G. Norman and G.R. Booker, *J. Appl. Phys.* **57**, 4715 (1985).
- <sup>3</sup>T.L. McDevitt, S. Mahajan, D.E. Laughlin, W.A. Bonner, and V.G. Keramidis, *Phys. Rev. B* **45**, 6614 (1992).
- <sup>4</sup>M. Tsuchiya, P.M. Petroff, and L.A. Coldren, *Appl. Phys. Lett.* **57**, 1690 (1989); M. Tsuchiya, J.M. Gaines, R.H. Yan, R.J. Simes, P.O. Holtz, L.A. Coldren, and P.M. Petroff, *Phys. Rev. Lett.* **62**, 466 (1989).
- <sup>5</sup>K. C. Hsieh, J. N. Baillargeon, and K. Y. Cheng, *Appl. Phys. Lett.* **57**, 2244 (1990).
- <sup>6</sup>A. C. Chen, A. M. Moy, P. J. Pearah, K. C. Hsieh, and K. Y. Cheng, *Appl. Phys. Lett.* **62**, 1359 (1993).
- <sup>7</sup>Y. Tang, H. T. Lin, D. H. Rich, P. Colter, and S. M. Vernon, *Phys. Rev. B* **53**, 10 501 (1996); D. H. Rich, Y. Tang, and H. T. Lin, *J. Appl. Phys.* **81**, 6837 (1997).
- <sup>8</sup>A. Mascarenhas, R. G. Alonso, G. S. Horner, S. Froyen, K. C. Hsieh, and K. Y. Cheng, *Superlattices Microstruct.* **12**, 57 (1992).
- <sup>9</sup>K. Y. Cheng, K. C. Hsieh, and J. N. Baillargeon, *Appl. Phys. Lett.* **60**, 2892 (1992).
- <sup>10</sup>S. T. Chou, K. Y. Cheng, L. J. Chou and K. C. Hsieh, *Appl. Phys. Lett.* **66**, 2220 (1995).
- <sup>11</sup>J. Mirecki Millunchick, R. D. Twesten, S. R. Lee, D. M. Follstaedt, E. D. Jones, S. P. Ahrenkiel, Y. Zhang, H. M. Cheong,

- and A. Mascarenhas, *MRS Bull.* **22**, 38 (1997).
- <sup>12</sup>J. Mirecki Millunchick, R. D. Twesten, D. M. Follstaedt, S. R. Lee, E. D. Jones, Y. Zhang, S. P. Ahrenkiel, and A. Mascarenhas, *Appl. Phys. Lett.* **70**, 1402 (1997).
- <sup>13</sup>J. Mirecki Millunchick, R. D. Twesten, S. R. Lee, D. M. Follstaedt, E. D. Jones, S. P. Ahrenkiel, Y. Zhang, H. M. Cheong, and A. Mascarenhas, *J. Electron. Mater.* **26**, 1048 (1997).
- <sup>14</sup>T. Y. Seong, A. G. Norman, I. T. Ferguson, and G. R. Booker, *J. Appl. Phys.* **73**, 8227 (1993).
- <sup>15</sup>S. W. Jun, T. Y. Seong, J. H. Lee, and B. Lee, *Appl. Phys. Lett.* **68**, 3443 (1996).
- <sup>16</sup>S.-J. Kim, H. Asahi, M. Takemoto, K. Asami, M. Takeuchi, and S. Gonda, *Jpn. J. Appl. Phys.* **35**, 4225 (1996).
- <sup>17</sup>J. Tersoff, C. Teichert, and M. G. Lagally, *Phys. Rev. Lett.* **76**, 1675 (1996).
- <sup>18</sup>A. G. Norman, S. P. Ahrenkiel, H. Moutinho, M. M. Al-Jassim, A. Mascarenhas, J. Mirecki Millunchick, S. R. Lee, R. D. Twesten, D. M. Follstaedt, J. L. Reno, and E. D. Jones, *Appl. Phys. Lett.* **73**, 1844 (1998).
- <sup>19</sup>B. J. Spencer, P. W. Voorhees, and S. H. Davis, *Phys. Rev. Lett.* **67**, 3696 (1991).
- <sup>20</sup>J. Tersoff, *Phys. Rev. Lett.* **77**, 2017 (1996).
- <sup>21</sup>I. P. Ipatovea, V. G. Malyshev, A. A. Maradudin, V. A. Shchukin, and R. F. Wallis, *Phys. Rev. B* **57**, 12 968 (1998).
- <sup>22</sup>Y. Zhang and A. Mascarenhas, *Phys. Rev. B* **57**, 12 245 (1998).
- <sup>23</sup>T. Mattila, L. Bellaiche, L.-W. Wang, and A. Zunger, *Appl. Phys. Lett.* **72**, 2144 (1998).

- <sup>24</sup>L.-W. Wang, L. Bellaiche, S.-H. Wei, and A. Zunger, *Phys. Rev. Lett.* **80**, 4725 (1998).
- <sup>25</sup>D. M. Wood and A. Zunger, *Phys. Rev. B* **53**, 7949 (1996).
- <sup>26</sup>P. N. Keating, *Phys. Rev.* **145**, 637 (1966); R. M. Martin, *Phys. Rev. B* **1**, 4005 (1970); J. L. Martins and A. Zunger, *ibid.* **30**, 6217 (1984).
- <sup>27</sup>A. Mascarenhas, Y. Zhang, J. Mirecki Millunchick, R. D. Twes-ten, and E. D. Jones, in *Future Generation Photovoltaic Technologies*, edited by R. D. McConnell, AIP Conf. Proc. No. 404 (AIP, New York, 1997), p. 303.
- <sup>28</sup>W. H. Press, B. P. Flannery, S. A. Teukolsky, and W. T. Vetterling, *Numerical Recipes* (Cambridge, New York, 1989).
- <sup>29</sup>C. Pryor, J. Kim, L.-W. Wang, A. Williamson, and A. Zunger, *J. Appl. Phys.* **83**, 2548 (1998).
- <sup>30</sup>J. R. Chelikowsky and M. L. Cohen, *Phys. Rev. B* **14**, 556 (1976).
- <sup>31</sup>A. Williamson, J. Kim, S.-H. Wei, L.-W. Wang, and A. Zunger (unpublished).
- <sup>32</sup>L.-W. Wang, J. Kim, and A. Zunger, *Phys. Rev. B* **59**, 5678 (1999).
- <sup>33</sup>L.-W. Wang and A. Zunger, *Phys. Rev. B* **51**, 17 398 (1995).
- <sup>34</sup>L.-W. Wang and A. Zunger, *J. Chem. Phys.* **100**, 2394 (1994); A. Zunger and L.-W. Wang, *Appl. Surf. Sci.* **102**, 350 (1996).
- <sup>35</sup>Our tests indicate that the size of the (110) planes is crucial for a realistic description of randomness of the alloy. For  $N=10$  we find that the absolute band-edge eigenvalues in our random alloy are converged better than 5 meV using a single sample in the calculations.
- <sup>36</sup>The cells used in modeling the band-edge energies contain 400 atoms in order to provide a realistic description of a random alloy. We use this approach instead of virtual crystal approximation (VCA) in order to avoid the problematic description of, e.g., strain effects and band gap bowing in VCA-type methods.
- <sup>37</sup>D. D. Sell, *Phys. Rev. B* **6**, 3750 (1972).
- <sup>38</sup>D. E. Aspnes and A. A. Studna, *Phys. Rev. B* **7**, 3607 (1973).
- <sup>39</sup>H. J. Drouhin, C. Hermann, and G. Lampel, *Phys. Rev. B* **31**, 3859 (1985).
- <sup>40</sup>T. C. Chiang, J. A. Knapp, M. Aono, and D. E. Eastman, *Phys. Rev. B* **21**, 3513 (1980).
- <sup>41</sup>W. Nakwaski, *Physica B* **210**, 1 (1995).
- <sup>42</sup>M. S. Skolnick, A. K. Jain, R. A. Stradling, L. Leotin, J. C. Ousset, and S. Ashkenazy, *J. Phys. C* **9**, 2809 (1976).
- <sup>43</sup>D. Olego, M. Cardona, and H. Muller, *Phys. Rev. B* **22**, 894 (1980).
- <sup>44</sup>A. Blacha, H. Presting, and M. Cardona, *Phys. Status Solidi B* **126**, 11 (1984).
- <sup>45</sup>R. P. Varfolpeev, P. Seisyan, and R. N. Yakimova, *Sov. Phys. Semicond.* **9**, 530 (1975).
- <sup>46</sup>L. Ley, R. A. Pollak, R. R. McFeely, S. P. Kowalczyk, and D. A. Sherlet, *Phys. Rev. B* **9**, 600 (1974).
- <sup>47</sup>R. R. Zucca and Y. R. Shen, *Phys. Rev. B* **1**, 2669 (1970).
- <sup>48</sup>L. M. Kanaskaya, S. I. Korhanovskii, R. P. Seisya, A. F. Efros, and V. A. Yukish, *Sov. Phys. Semicond.* **17**, 449 (1983).
- <sup>49</sup>Y. J. Jung, B. H. Kim, H. J. Lee, and J. C. Woolley, *Phys. Rev. B* **26**, 3151 (1982).
- <sup>50</sup>C. R. Pidgeon, S. H. Groves, and J. Feinleib, *Solid State Commun.* **5**, 677 (1967).
- <sup>51</sup>X. Zhu and S. G. Louie, *Phys. Rev. B* **43**, 14 142 (1991).
- <sup>52</sup>D. S. Kyser and V. Rehn, *Phys. Rev. Lett.* **40**, 1038 (1978).
- <sup>53</sup>D. E. Aspnes, C. G. Olson, and D. W. Lynch, *Phys. Rev. B* **12**, 1371 (1975).
- <sup>54</sup>S.-G. Shen and X.-Q. Fan, *J. Phys.: Condens. Matter* **8**, 4369 (1996).
- <sup>55</sup>J. R. Chelikowsky and M. L. Cohen, *Phys. Rev. B* **14**, 556 (1976).
- <sup>56</sup>R. G. Humphreys, U. Rossler, and M. Cardona, *Phys. Rev. B* **18**, 5590 (1978).
- <sup>57</sup>D. F. Nelson, L. F. Johnson, and M. Gershenson, *Phys. Rev.* **135**, A1399 (1964).
- <sup>58</sup>J. Camassel, P. Merle, L. Bayo, and H. Mathieu, *Phys. Rev. B* **22**, 2020 (1980).
- <sup>59</sup>G.P. Williams, F. Cerrina, J. Anderson, G. J. Lapeyre, R. J. Smith, J. Hermanson, and J. A. Knapp, *Physica B & C* **117&118**, 350 (1983).
- <sup>60</sup>A. Onton, R. J. Chicotka, and Y. Yacoby, *Proceedings of the Eleventh International Conference on Physics and Semiconductors* (Polish Scientific Publishers, Warsaw, 1972), p. 1023.
- <sup>61</sup>E. Matatagui, A. E. Thompson, and M. Cardona, *Phys. Rev.* **176**, 950 (1968).
- <sup>62</sup>L. W. James, J. P. van Dyke, F. Herman, and D. M. Chang, *Phys. Rev. B* **1**, 3998 (1970).
- <sup>63</sup>M. Helm, W. Knap, W. Seidenbusch, R. Lassnig, and E. Gornik, *Solid State Commun.* **53**, 547 (1985).
- <sup>64</sup>J. Leotin, R. Barbaste, S. Askenazy, R. A. Stradling, and J. Tuchendler, *Solid State Commun.* **15**, 693 (1974).